Frontiers in Bioscience Landmark

Front. Biosci. (Landmark Ed) **2026**; 31(9): 54017
https://doi.org/10.31083/FBL54017

Original Research

3D-Printed DOX-LF-Loaded PLGA Biphasic Composite Scaffold Modulates Macrophage Polarization and Enhances Osteogenic-Angiogenic Regenerative Potential for Periodontitis

Chunfeng Wang[1,†], Caijuan Wu[2,†], Chan Xiao[1], Yepo Hou[1,*]

[1]Department of Stomatology, Hunan University of Medicine, 418000 Huaihua, Hunan, China
[2]Department of Stomatology, The Eighth Affiliated Hospital, Southern Medical University (The First People's Hospital of Shunde, Foshan), 528308 Foshan, Guangdong, China
*Correspondence: m15111509223@163.com (Yepo Hou)
[†]These authors contributed equally.

Academic Editor: Francesca Diomede
Submitted: 19 May 2026 Revised: 20 July 2026 Accepted: 27 July 2026 Published: 18 September 2026

Abstract

Background: To develop an immunomodulatory scaffold integrating antibacterial activity with osteogenic–angiogenic coupling for inflammatory periodontal repair. **Methods:** A biphasic poly(lactic-co-glycolic acid) (PLGA) scaffold incorporating doxycycline-lactoferrin (DOX-LF)-loaded calcium alginate microspheres and fibroblast growth factor 2/bone morphogenetic protein 9 (FGF2/BMP9)-loaded chitosan nanospheres was fabricated by low-temperature three-dimensional (3D) printing, porogen leaching, and freeze-drying. Material properties, antibacterial activity, macrophage polarization, periodontal ligament stem cell (PDLSC) osteogenesis, and human umbilical vein endothelial cell (HUVEC) angiogenesis were evaluated. Small interfering RNA (siRNA)-mediated milk fat globule-epidermal growth factor 8 (MFGE8) knockdown was used to investigate the underlying mechanism. **Results:** The scaffold formed an interconnected porous network and released approximately 88.4% of DOX and 60% of LF over 240 h. PLGA/DOX-LF reduced Porphyromonas gingivalis viability to approximately 20% ($p < 0.001$). In lipopolysaccharide (LPS)-stimulated macrophages, it produced the greatest suppression of M1-associated markers and induction of M2-associated markers, while MFGE8 knockdown significantly reduced MFGE8 expression ($p < 0.001$) and attenuated these effects. Conditioned medium restored PDLSC migration, ALP activity, and mineralization to approximately 70%, 70–75%, and 80% of control levels, respectively, and increased HUVEC tube length ($p < 0.01$) and angiogenic gene expression (all $p < 0.001$). **Conclusions:** A 3D-printed biphasic PLGA scaffold incorporating DOX-LF-loaded calcium alginate microspheres and FGF2/BMP9-loaded chitosan nanospheres was successfully constructed. These *in vitro* findings support PLGA/DOX-LF as a proof-of-concept platform for antibacterial immunomodulation and osteogenic–angiogenic coupling, pending *in vivo* validation.

Keywords: inflammatory periodontal tissue defect; PLGA/DOX-LF scaffold; macrophage polarization; osteogenesis-angiogenesis coupling; MFGE8

1. Introduction

Periodontitis is a chronic biofilm-associated inflammatory disease characterized by progressive destruction of the periodontal ligament and alveolar bone [1]. Rather than resulting from a single pathogen, disease initiation and progression reflect a shift from a symbiotic oral microbiota toward a dysbiotic community that perturbs host-microbe homeostasis. Keystone and pathobiont species can amplify inflammatory signaling, alter local nutrient conditions, and sustain a destructive immune response [2,3]. Similar ecological disruption occurs around dental implants, although peri-implant biofilms develop on distinct surfaces and may contain a broader range of opportunistic microorganisms [4,5]. Consequently, periodontitis and peri-implantitis are increasingly regarded as dysbiosis-driven inflammatory disorders in which microbial imbalance and unresolved host responses reinforce each other.

Macrophages are central regulators of this interaction. During active inflammation, M1-like macrophages produce inducible nitric oxide synthase, tumor necrosis factor-α, interleukin-1β, and other mediators that promote matrix degradation and osteoclastogenesis [6]. Conversely, M2-like macrophages secrete anti-inflammatory and reparative factors, including interleukin-10, transforming growth factor-β, and angiogenic mediators, thereby supporting inflammation resolution, vascularization, and tissue reconstruction [7]. Clinical and experimental evidence indicates that an increased M1/M2 balance is associated with periodontal destruction [8], suggesting that coordinated control of infection and macrophage phenotype may be more effective than strategies directed exclusively at bacterial elimination [9].

Current periodontal and peri-implant therapies primarily rely on mechanical biofilm disruption, with antiseptics or systemic/local antibiotics used in selected cases

[10]. However, recent evidence emphasizes that antimicrobial therapy does not uniformly restore a health-associated microbiome [11,12]. A recent systematic review and meta-analysis found no additional clinical or microbiological benefit of systemic antibiotics for peri-implant mucositis and only limited improvements in selected peri-implantitis outcomes, without consistent marginal bone-level benefits [13]. This finding highlights the need for antibiotic stewardship, particularly because repeated or empirical antibiotic exposure may select resistant organisms and disturb commensal communities. Microbiome-directed strategies-including probiotics, prebiotics, phage-related approaches, and ecological modulation-have therefore attracted interest as adjuncts to mechanical therapy, although their clinical effects remain heterogeneous and long-term evidence is still limited [14,15,16].

Biomaterial-mediated immune regulation provides a new paradigm for periodontal tissue regeneration. 3D printing technology can precisely control scaffold pore structure, mechanical properties, and drug release kinetics. This capability significantly influences macrophage behavior. Studies show that scaffold pore size can directly regulate macrophage polarization direction. Large-pore polyether ether ketone (PEEK) scaffolds more easily induce M1 to M2 transformation and enhance pro-angiogenic factor secretion [17]. Physical properties such as fiber orientation and surface topography can also guide macrophages toward repair phenotypes through signaling pathways including Yes-associated protein/transcriptional coactivator with PDZ-binding motif (YAP/TAZ) and phosphoinositide 3-kinase/protein kinase B/β-catenin (PI3K/AKT/β-catenin) [18,19,20]. At the materials chemistry level, multiple functionalization strategies have proven effective. Mannose-modified nano-hydroxyapatite (GHANPs) promotes M2 polarization by regulating mitochondrial oxidative phosphorylation and autophagy [8]. Magnetic superparamagnetic iron oxide nanoparticles (SPIONs)/Poly(lactic-co-glycolic acid) (PLGA) scaffolds achieve effective bone repair in infectious microenvironments through antibacterial and anti-adhesion properties. They reduce NOD-like receptor family pyrin domain containing 3 (NLRP3)/interleukin-1β (IL-1β) expression and elevate interleukin-10 (IL-10) levels [21]. These advances highlight the central role of the "material-immunity-regeneration" axis in periodontal tissue engineering.

However, existing scaffold designs still face dual challenges. Reactive oxygen species (ROS) accumulation and persistent infection in inflammatory microenvironments easily lead to M1 polarization dominance. This hinders repair progression [22,23]. Insufficient spatiotemporal coupling between osteogenesis and angiogenesis often causes regenerative failure due to inadequate blood supply in newly formed bone tissue [7,24]. Ideal scaffolds need both "sequential immune regulation" and "functional synergy" capabilities. They should rapidly suppress excessive inflammation early, promote M2 macrophages to secrete vascular endothelial growth factor (VEGF), platelet-derived growth factor (PDGF), and other factors to drive angiogenesis in the middle stage, and synergistically activate osteogenic differentiation of bone marrow mesenchymal stem cells (BMSCs)/periodontal ligament stem cells (PDLSCs) in the late stage [22,24]. M2 macrophage-conditioned medium has been confirmed to significantly enhance the tube formation capacity of human umbilical vein endothelial cells and the mineralized nodule formation of bone marrow mesenchymal stem cells [19,24]. This suggests a cascade regulatory relationship among "macrophage polarization-angiogenesis-bone regeneration". Additionally, exosomes (such as M2-EVs and human periodontal ligament stem cell-derived apoptotic extracellular vesicles [hPDLSCs-ApoEVs]) regulate macrophage phenotypes through pathways including nuclear factor kappa-B (NF-κB)/S100 calcium-binding protein A9 (S100A9). This provides new ideas for cell-free therapy [25]. However, their *in vivo* stability and controlled release strategies still require carrier optimization.

Poly(lactic-co-glycolic acid) is a biodegradable and clinically relevant polymer with tunable mechanical and drug-release properties [26,27]. Doxycycline provides broad antimicrobial activity and may suppress matrix-degrading and inflammatory pathways, whereas lactoferrin has antibacterial, iron-binding, and immunoregulatory functions [28,29]. Their localized co-delivery may reduce bacterial burden while promoting a reparative immune microenvironment, potentially avoiding the limitations of prolonged systemic antibiotic exposure. However, whether a three-dimensional PLGA scaffold carrying doxycycline and lactoferrin can couple macrophage reprogramming with osteogenic and angiogenic responses remains insufficiently defined.

Accordingly, this study developed a low-temperature three-dimensional (3D)-printed PLGA scaffold loaded with doxycycline and lactoferrin. We characterized its morphology, chemical composition, mechanical behavior, drug loading and release, and antibacterial activity. We further examined its effects on lipopolysaccharide (LPS)-induced RAW264.7 macrophage polarization and investigated whether macrophage-conditioned medium influenced periodontal ligament stem cell migration and osteogenic differentiation and endothelial tube formation. Finally, milk fat globule-epidermal growth factor 8 (MFGE8) knockdown was used to assess its contribution to scaffold-mediated macrophage reprogramming. This study aims to provide a proof-of-concept for a multifunctional scaffold that integrates immune regulation with tissue regeneration, offering a new strategy for repairing inflammatory periodontal defects.

2. Materials and Methods

2.1 Experimental Materials

Reagents: Poly(lactic-co-glycolic acid) (PLGA, molecular weight 50,000–75,000 Da, lactic acid:glycolic acid = 85:15, 430471), doxycycline hydrochloride (DOX, D9891), and lactoferrin (LF, L9507) were purchased from Sigma-Aldrich (Saint Louis, MO, USA). Dichloromethane (DCM, 75-09-2), N, N-dimethylformamide (DMF, 68-12-2), 1,4-butanediol diacrylate (BDDA, 1070-70-8), polyethylene glycol 400 (PEG400, 25322-68-3), and sodium chloride (NaCl, 7647-14-5) were all analytical grade and purchased from Sinopharm Chemical Reagent Co., Ltd (Shanghai, China). Sodium alginate (9005-38-3) and calcium chloride (10043-52-4) were purchased from Aladdin Reagent Company (Shanghai, China).

RAW264.7 mouse macrophage cell line (CL-0190), human umbilical vein endothelial cells (HUVECs, CP-H082Y), and mouse periodontal ligament stem cells (PDLSCs, CP-M325) were purchased from Procell (Wuhan, Hubei, China). Cell identities were verified by supplier certificates and characteristic morphology/marker profiles. All cultures tested negative for mycoplasma using a PCR-based detection kit before experimentation. *Porphyromonas gingivalis* lipopolysaccharide (*P.g.*-LPS, tlrl-pglps) was obtained from InvivoGen (San Diego, CA, USA).

Recombinant fibroblast growth factor 2 (FGF2; Cat. No. 3139-FB) and bone morphogenetic protein 9 (BMP9; Cat. No. 5566-BP) were purchased from Bio-Techne (Minneapolis, MN, USA). For immunofluorescence staining of macrophages, the following antibodies were used: rabbit anti-mouse cluster of differentiation 86 (CD86) antibody (ab305361; Abcam, Cambridge, Cambridgeshire, UK), Alexa Fluor 488-conjugated rabbit anti-mouse cluster of differentiation 206 (CD206) antibody (ab318602; Abcam; Cambridge, Cambridgeshire, UK), goat anti-rabbit immunoglobulin G (IgG) conjugated to Alexa Fluor 594 (A-11012; Invitrogen;Thermo Fisher Scientific; Waltham, MA, USA), and 4′,6-diamidino-2-phenylindole (DAPI) (D1306; Invitrogen, Thermo Fisher Scientific; Waltham, MA, USA).

The Cell Counting Kit-8 (CCK-8) assay kit (CK04) and Calcein-AM/Propidium Iodide (PI) double staining kit (CS01), used for cell viability staining, were purchased from Dojindo Laboratories (Mashiki, Kumamoto, Japan). The LIVE/DEAD BacLight Bacterial Viability Kit (L7012), used for bacterial live/dead staining, was purchased from Invitrogen, Thermo Fisher Scientific (Waltham, MA, USA). Total RNA was extracted using TRIzol reagent (15596026; Invitrogen, Thermo Fisher Scientific; Waltham, MA, USA). The PrimeScript RT kit (RR047A), and TB Green Premix Ex Taq II (RR820A) were purchased from TaKaRa (Kusatsu, Shiga, Japan). Alkaline phosphatase (ALP) staining kit (PCM-K-002; zqxzbio Biotechnology; Shanghai, China), Alizarin Red S Staining Kit (C0148S; Beyotime; Shanghai, China), and MFGE8 enzyme-linked immunosorbent assay (ELISA) kit (ORSE922M; Aopusa Biotechnology; Wuhan, Hubei, China) were also used. Small interfering RNA targeting *MFGE8* (si-*MFGE8*), negative control small interfering RNA (si-NC), and reverse transcription-quantitative polymerase chain reaction (RT-qPCR) primers were purchased from Sangon Biotech (Shanghai, China).

Main instruments: The principal instruments included a fused deposition modeling (FDM) 3D printer (E2; Raise3D Technologies; Stafford, Texas, USA), a screw-extrusion 3D bioprinter (Bio-Architect; Regenovo Biotechnology Co., Ltd.; Hangzhou, Zhejiang, China), a freeze dryer (Alpha 1-4 LD plus; Martin Christ Gefriertrocknungsanlagen GmbH; Osterode am Harz, Lower Saxony, Germany), and a field-emission scanning electron microscope equipped with an energy-dispersive X-ray spectroscopy (EDS) detector (SU8010; Hitachi High-Tech Corporation; Tokyo, Japan).

Specific surface area and pore-size measurements were performed using an automated surface-area and porosimetry system (ASAP 2460; Micromeritics Instrument Corporation; Norcross, GA, USA). Fourier-transform infrared spectroscopy (FT-IR), X-ray photoelectron spectroscopy (XPS), and Raman measurements were conducted using a Nicolet iS50 FT-IR spectrometer (Thermo Fisher Scientific; Waltham, MA, USA), a K-Alpha X-ray photoelectron spectrometer (Thermo Fisher Scientific; Waltham, MA, USA), and a LabRAM HR Evolution confocal Raman microscope (HORIBA France SAS; Palaiseau, France), respectively. The ASAP 2460 is an automated surface-area and porosimetry platform, whereas the K-Alpha and LabRAM HR Evolution are dedicated XPS and Raman systems.

Fluorescence images were acquired using a laser-scanning confocal microscope (LSM 880; Carl Zeiss Microscopy GmbH; Jena, Thuringia, Germany) or an inverted fluorescence microscope (ECLIPSE Ti2-U; Nikon Corporation, Tokyo, Japan). RT-qPCR was performed using a CFX96 Touch Real-Time PCR Detection System (Bio-Rad Laboratories; Hercules, CA, USA).

2.2 3D Printing Preparation of PLGA Biphasic Composite Scaffolds

(1) Printing paste preparation: Accurately weigh 2 g PLGA granules. Add 10 mL DCM/DMF mixed solvent (volume ratio 9:1). Stir magnetically at 30 °C for 1–1.5 h until completely dissolved. Add NaCl particles (100–200 μm) at a PLGA: NaCl mass ratio of 1:3 as a porogen. Add BDDA at 1% of PLGA mass as a crosslinking agent and PEG400 at 5% as a plasticizer. Disperse uniformly with ultrasound assistance (150 W, 5 min). At 30 °C, adjust paste viscosity to 30,000–50,000 mPa·s by adding DCM or DMF. Degas for 30 min at 0.08 MPa vacuum to obtain homogeneous printing paste.

(2) Mold design and printing: Based on the target tooth defect morphology, construct three-dimensional mold models with arc structures using computer-aided design (CAD) software (SOLIDWORKS 2022; Dassault Systèmes; Vélizy-Villacoublay, Île-de-France, France). Molds were printed using polylactic acid (PLA) filament through FDM 3D printer. Printing parameters were: nozzle temperature 190 °C, platform temperature 50 °C, printing speed 30 mm/s, layer thickness 0.2 mm. Printed molds were annealed at 75 °C for 2 h to eliminate internal stress.

(3) Scaffold molding and post-processing: Load prepared PLGA printing paste into the screw-type 3D printer barrel. Use an FDM-printed PLA mold as a substrate for extrusion molding. Printing parameters were: ambient temperature 25 °C, nozzle diameter 0.4 mm, layer thickness 0.1 mm, printing speed 20 mm/s, using an arc layered path. Allow to stand for 6 h for solidification in the mold. Carefully demold to obtain the scaffold green body. Place the scaffold green body in deionized water at 25 °C. Stir magnetically at 150 rpm for porogen leaching. Change water every 2 h for 12 h until no white precipitate (Cl^-) is detected with 0.1 M $AgNO_3$ solution. Pre-freeze leached scaffolds at –40 °C for 2 h. Then place in a freeze dryer at 5 Pa vacuum and –50 °C for 8 h to obtain final porous scaffolds. Disinfect scaffolds by soaking in 75% ethanol for 30 min. Rinse with sterile PBS 3 times for standby use.

2.3 Drug Loading and Scaffold Composition

(1) Calcium alginate hydrogel encapsulation of DOX-LF: Dissolve DOX and LF at a mass ratio of 1:1 in 1% (w/v) sodium alginate solution. Use a high-voltage electrostatic droplet generator to drip mixed solution into 100 mM $CaCl_2$ solution. Form microspheres with uniform particle size. Collect microspheres. Wash with deionized water three times. Freeze-dry to obtain DOX-LF-loaded calcium alginate hydrogel microspheres.

(2) Preparation of FGF2/BMP9chitosan nanospheres: Use the ionic crosslinking method. Dissolve FGF2 and BMP9 (mass ratio 1:1) in 0.2% (w/v) chitosan solution. Slowly drip into 0.1% (w/v) sodium tripolyphosphate solution under stirring to form drug-loaded nanospheres. Collect nanospheres by centrifugation (12,000 rpm, 30 min). Freeze-dry for standby use.

(3) Composite scaffold construction: Uniformly suspend prepared DOX-LF calcium alginate microspheres and FGF2/BMP9 chitosan nanospheres (mass ratio 1:2) in PLGA printing paste. Then proceed with 3D printing and scaffold molding according to section 2.2. Finally, obtain PLGA biphasic composite scaffolds co-loaded with DOX-LF and FGF2/BMP9 (hereinafter referred to as PLGA/DOX-LF).

2.4 Physicochemical Characterization of Scaffold Materials

The morphology and hierarchical pore architecture of the fabricated scaffolds were examined by scanning electron microscopy (SEM) at an accelerating voltage of 5 kV. Before imaging, freeze-dried samples were mounted on conductive stubs and sputter-coated with gold. Images were acquired at progressively increasing magnifications to evaluate macropore morphology, pore-wall integrity, surface roughness, and pore interconnectivity. Elemental composition and spatial distribution were further analyzed by EDS coupled to the SEM.

Nitrogen adsorption-desorption measurements were performed using an automated surface-area and porosity analyzer after vacuum degassing. The specific surface area was calculated using the Brunauer-Emmett-Teller method, and pore-size distributions were obtained using the Barrett-Joyner-Halenda model. Chemical structures were characterized by Fourier-transform infrared spectroscopy over 400–4000 cm^{-1} at a resolution of 4 cm^{-1}. Raman spectra were recorded using a 532-nm excitation laser to examine characteristic molecular vibrations. Surface elemental composition and chemical bonding states were evaluated by X-ray photoelectron spectroscopy using monochromatic Al Kα radiation (hν = 1486.6 eV). Survey spectra and high-resolution C1s and O1s spectra were collected and subjected to peak deconvolution.

Thermal stability was assessed by thermogravimetric and derivative thermogravimetric analyses under nitrogen from 25 to 600 °C at a heating rate of 10 °C/min. Compressive properties were evaluated by quasi-static uniaxial compression, and the elastic modulus was calculated from the initial linear region of the stress-strain curve. Doxycycline and lactoferrin contents were quantified by validated high-performance liquid chromatography (HPLC) methods using concentration-peak area calibration curves. *In vitro* release was monitored for 240 h, and cumulative release data were fitted to zero-order, first-order, Higuchi, and Ritger-Peppas models. All measurements were performed using three independent scaffold samples.

2.5 Antibacterial Performance Evaluation

Porphyromonas gingivalis (*P. gingivalis*) American Type Culture Collection (ATCC) 33277 was obtained from the American Type Culture Collection (Manassas, VA, USA) and cultured in supplemented tryptic soy broth at 37 °C under anaerobic conditions (80% N_2, 10% H_2, and 10% CO_2). Log-phase bacteria were adjusted to 1×10^8 colony-forming units per milliliter (CFU). Equal-sized sterile scaffolds were incubated with 1 mL bacterial suspension for 24 h. The groups were Control, PLGA, PLGA/DOX, PLGA/LF, and PLGA/DOX-LF. After gentle washing with sterile saline, bacteria were stained using the LIVE/DEAD BacLight Bacterial Viability Kit (L7012; Invitrogen, Carlsbad, CA, USA) for 15 min in the dark. Viable and

membrane-compromised bacteria appeared green and red, respectively. Green fluorescence was quantified using ImageJ (National Institutes of Health, Bethesda, MD, USA) and normalized to the Control group. Three independent scaffold samples were analyzed per group.

2.6 Cell Culture and Treatment

Mouse macrophage cell line RAW264.7, mouse PDLSCs, HUVECs. RAW264.7 cells and HUVECs were cultured in DMEM high-glucose medium. PDLSCs were cultured in alpha-Minimum Essential Medium (α-MEM) (12571063; Gibco, Thermo Fisher Scientific; Paisley, Scotland, UK). All media were supplemented with 10% fetal bovine serum (FBS) and 1% penicillin-streptomycin solution. Incubate at 37 °C, 5% CO_2. Change medium every 2–3 days. Passage when cell confluence reaches 80%–90%.

Scaffold extracts were prepared at 0.2 g/mL using the medium appropriate for each cell type. Scaffolds were incubated at 37 °C for 24 h, and the extracts were centrifuged and sterilized through 0.22-μm filters. RAW264.7 cells were assigned to the Control, LPS, LPS + PLGA, LPS + PLGA/DOX, LPS + PLGA/LF, and LPS + PLGA/DOX-LF groups. Inflammatory polarization was induced using 1 μg/mL *P.g.*-LPS for 24 h, followed by treatment with the corresponding scaffold extract for another 24 h.

2.7 Cell Viability and Live/Dead Staining

RAW264.7 cells, PDLSCs, or HUVECs were seeded in 96-well plates at 5×10^3 cells/well and cultured overnight. After treatment with scaffold extracts or macrophage-conditioned media for 24 h, 10 μL of CCK-8 reagent was added to each well. After incubation for 2 h at 37 °C, absorbance was measured at 450 nm. Cell viability was normalized to the untreated Control group.

For direct cytocompatibility assessment, PDLSCs or HUVECs were incubated with scaffold extracts and subjected to Calcein-AM/PI live/dead staining according to the manufacturer's protocol. Five random fields were acquired using identical exposure parameters. Each experiment included three independent biological replicates, with three technical wells per replicate.

2.8 Macrophage Immunofluorescence

RAW264.7 cells were seeded on coverslips in 24-well plates at 2×10^5 cells/well. Following treatment, cells were fixed with 4% paraformaldehyde for 15 min, permeabilized with 0.2% Triton X-100 for 10 min, and blocked with 5% bovine serum albumin for 30 min. Cells were incubated overnight at 4 °C with rabbit anti-mouse CD86 antibody. CD86 was visualized using an Alexa Fluor 594-conjugated goat anti-rabbit secondary antibody. CD206 was detected using an Alexa Fluor 488-conjugated anti-mouse CD206 antibody. Nuclei were counterstained with DAPI. Images were acquired using identical laser power, gain, and exposure settings. Mean fluorescence intensity was quantified from 5 random fields.

2.9 RNA Extraction and RT-qPCR

Total RNA was extracted using TRIzol and quantified by spectrophotometry. Samples with A260/A280 ratios of 1.8–2.0 were used. One microgram of RNA was reverse-transcribed using the PrimeScript RT kit. RT-qPCR was performed using TB Green Premix Ex Taq II on a CFX96 system in 20-μL reactions containing 10 μL of 2× master mix, 0.4 μL each of forward and reverse primers at 10 μM, 2 μL of diluted cDNA, and nuclease-free water. Cycling conditions were 95 °C for 30 s, followed by 40 cycles of 95 °C for 5 s and 60 °C for 30 s. Melt-curve analysis was performed to verify amplification specificity. No-template and no-reverse-transcription controls were included. Reactions were performed in technical triplicate, and relative expression was calculated using the $2^{-\Delta\Delta Ct}$ method with species-matched *GAPDH* as the reference gene.

2.10 Macrophage-Conditioned Medium and Functional Assays

(1) Collection of macrophage-conditioned medium: After macrophage treatment, the medium was replaced with serum-free DMEM, and cells were cultured for another 24 h. Supernatants were centrifuged at 1000 ×g for 5 min and passed through 0.22-μm filters. Conditioned medium (CM) was mixed 1:1 with fresh complete medium before PDLSC or HUVEC treatment.

(2) Cell migration ability detection: For migration assays, 5×10^4 PDLSCs in serum-free medium were seeded into 8-μm Transwell inserts. The lower chamber contained 500 μL of medium supplemented with the corresponding CM. After 24 h, non-migrated cells were removed; migrated cells were fixed with 4% paraformaldehyde, stained with 0.1% crystal violet, and counted in five random fields.

(3) ALP staining and Alizarin Red S staining: For osteogenic evaluation, PDLSCs were cultured with CM-containing osteogenic medium supplemented with 10 mM β-glycerophosphate and 50 μg/mL ascorbic acid. ALP staining and activity measurement were performed after 7 days. Activity was measured at 405 nm and normalized to total protein. Alizarin Red S staining was performed after 14 days. Cells were fixed, stained with 2% Alizarin Red S at pH 4.2 for 20 min, and imaged. Bound dye was dissolved in 10% cetylpyridinium chloride and measured at 562 nm.

(4) Tube formation assay: Coat Matrigel basement membrane matrix (Corning) in pre-cooled 96-well plates at 50 μL/well. Incubate at 37 °C for 30 min to solidify. Seed HUVECs on the Matrigel surface at 2×10^4 cells/well. Add conditioned medium from each group. Culture for 6 h. Observe and photograph in 5 random fields under an inverted microscope. The total tube length was quantified using the Angiogenesis Analyzer plugin in ImageJ to evaluate the angiogenic capacity of HUVECs.

2.11 MFGE8 Knockdown and ELISA Assays

RAW264.7 cells were seeded in antibiotic-free medium and transfected at 30%–50% confluence. Small interfering RNA targeting milk fat globule-epidermal growth factor 8 (si-*MFGE8*) and negative control small interfering RNA (si-NC) were used, with their sequences listed in Table 1. The siRNAs were diluted in Opti-MEM and complexed with Lipofectamine RNAiMAX for 10–20 min. For a 24-well plate, 6 pmol siRNA and 1 µL RNAiMAX were added per well, yielding an initial final siRNA concentration of 10 nM. Cells were incubated for 24–48 h before knockdown validation. The primer sequences used for RT-qPCR are provided in **Supplementary Table 1**.

Table 1. siRNA oligonucleotide sequences.

Oligonucleotide	Strand	Sequence (5′–3′)
si-*MFGE8*	Sense	CCAAAUGUCUGGUGACUUUTT
si-*MFGE8*	Antisense	AAAGUCACCAGACAUUUGGTT
si-NC	Sense	UUCUCCGAACGUGUCACGUTT
si-NC	Antisense	ACGUGACACGUUCGGAGAATT

si-*MFGE8*, small interfering RNA targeting milk fat globule-epidermal growth factor 8; si-NC, negative control small interfering RNA.

MFGE8 protein secretion was quantified using a commercial mouse MFGE8 ELISA kit according to the manufacturer's instructions. After the indicated treatments, RAW264.7 cell supernatants were collected, centrifuged at 1000 ×g for 10 min to remove cellular debris, and stored at –80 °C until analysis. Standards and diluted samples were added to antibody-coated wells and sequentially incubated with the detection antibody and horseradish peroxidase conjugate. After washing, 3,3′,5,5′-tetramethylbenzidine (TMB) substrate was added, and the reaction was terminated with stop solution. Absorbance was measured at 450 nm, and MFGE8 concentrations were calculated from the standard curve.

2.12 Statistical Analysis

Data are presented as mean ± SD. The biological replicate number represents independently cultured cells or independently prepared scaffold batches rather than repeated measurements from the same sample. Technical replicates were averaged before statistical analysis. In this study, all experiments included at least three biological replicates. Normality and variance homogeneity were assessed using the Shapiro-Wilk and Brown-Forsythe tests, respectively. Two-group comparisons were performed using an unpaired two-tailed Student's *t*-test. Multiple-group comparisons were performed using one-way analysis of variance (ANOVA) followed by Tukey's multiple-comparison test. When assumptions were not met, corresponding nonparametric tests were used. Analyses were performed using GraphPad Prism 9.0 (GraphPad Software, LLC, San Diego, CA, USA), with $p < 0.05$ considered statistically significant.

3. Results

3.1 Preparation and Characterization of 3D Printed PLGA Scaffold Materials

A PLGA scaffold was successfully fabricated by combining low-temperature 3D printing, porogen leaching, and freeze-drying. SEM images acquired at progressively increasing magnifications revealed a well-developed 3D interconnected macroporous network (Fig. 1A–D). At low magnification, the scaffold displayed abundant open pores with extensive interconnectivity (Fig. 1A). Higher-magnification images confirmed that the pore walls remained continuous and structurally intact, without obvious collapse or fracture (Fig. 1B,C). At the nanoscale, the scaffold struts exhibited a distinctly rough and heterogeneous surface topography (Fig. 1D), which may provide additional interfacial area for drug loading and cell attachment.

EDS elemental mapping demonstrated dense and homogeneous distributions of carbon and oxygen throughout the selected scaffold region (Fig. 1E,F), in agreement with the elemental composition of PLGA. By contrast, Na, Cl, and N signals were sparse and close to background levels (Fig. 1G–I), suggesting minimal residual impurities. The XPS survey spectrum showed two predominant peaks corresponding to C1s and O1s (Fig. 1J). Deconvolution of the high-resolution C1s spectrum identified components at approximately 285.0, 287.0, and 289.0 eV, assigned to C-C/C-H, C-O, and O-C=O bonds, respectively (Fig. 1K). The O1s spectrum was resolved into peaks centered at approximately 532.5 and 533.5 eV, corresponding to O=C and C–O species (Fig. 1L). These findings were consistent with the characteristic polyester structure of PLGA. FT-IR analysis further revealed an intense carbonyl stretching band at 1745 cm^{-1}, prominent C–O–C stretching bands between 1082 and 1269 cm^{-1}, and weaker C–H stretching bands near 2951 and 2999 cm^{-1} (Fig. 1N). The Raman spectrum also displayed a high-wavenumber band tentatively assigned to C–H vibration, supporting preservation of the PLGA molecular framework (Fig. 1M).

The drug-loaded scaffold exhibited a hierarchical porous architecture, with a total porosity of approximately 80% (**Supplementary Tables 2,3**). The nitrogen adsorption-desorption isotherm displayed a typical type IV profile with a closed hysteresis loop at $P/P_0 \approx 0.6$–0.9. Barrett-Joyner-Halenda (BJH) analysis showed a broad pore-size distribution of approximately 2–400 nm, with a dominant peak near 290 nm, confirming mesopores and larger interconnected channels (Fig. 2A). Thermogravimetric-derivative thermogravimetric (TG-DTG) analysis revealed minimal mass loss below 250 °C, followed by rapid degradation between 280 and 350 °C, with a maximum degradation rate near 320 °C (Fig. 2B). In compression testing, the stress-strain curve was lin-

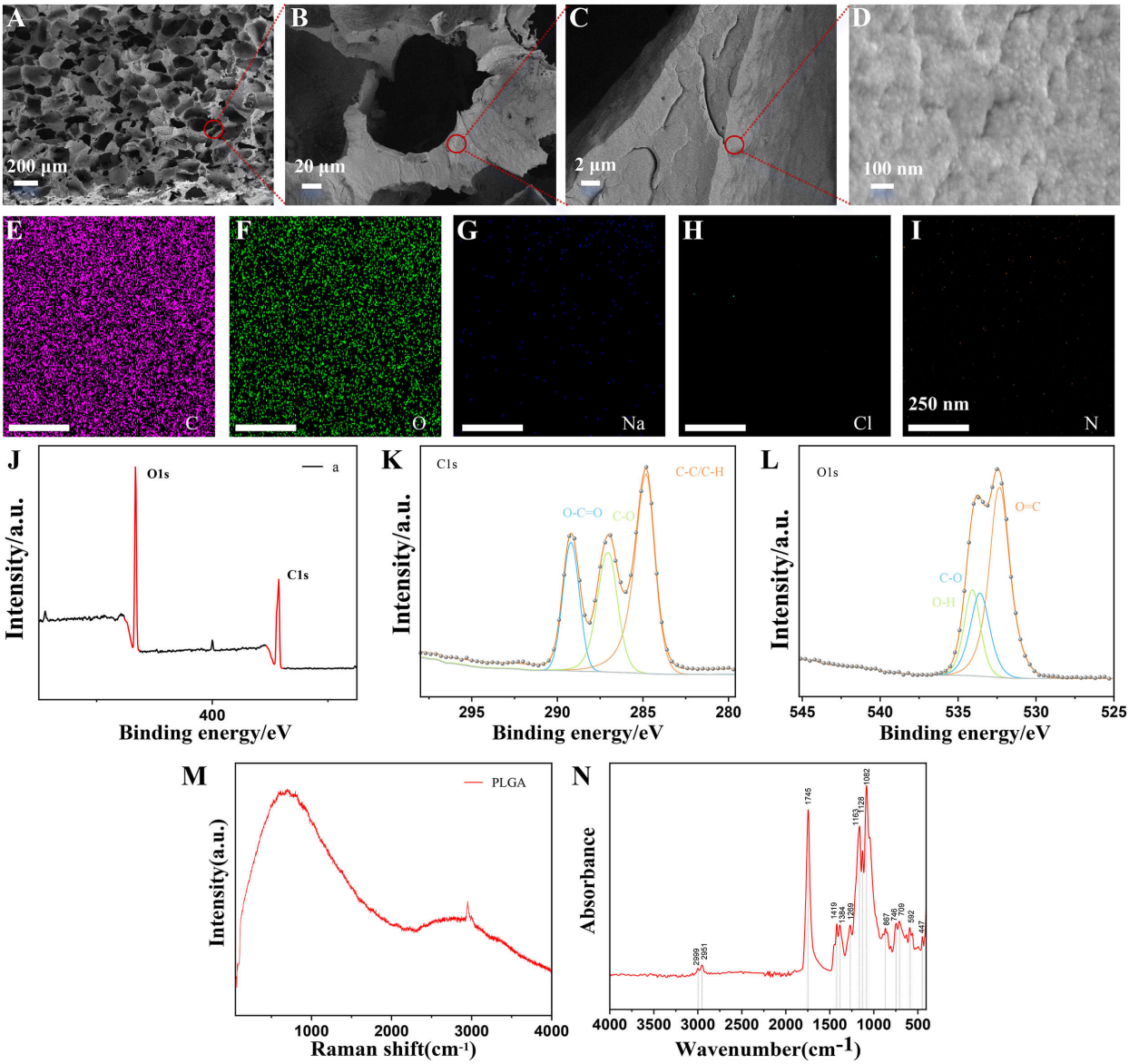

Fig. 1. Morphological and chemical characterization of the 3D-printed PLGA scaffold. (A–D) SEM images acquired at increasing magnifications, showing the interconnected macroporous architecture, preserved pore-wall integrity, and rough scaffold surface. Scale bars: 200 μm (A), 20 μm (B), 2 μm (C), and 100 nm (D). (E–I) EDS elemental maps of C, O, Na, Cl, and N. Scale bars = 250 nm. (J) XPS survey spectrum. (K,L) High-resolution C1s and O1s spectra with peak deconvolution. (M,N) Raman and FT-IR spectra confirming the characteristic molecular structure of PLGA. n = 3 independent replicates. Scale bars are indicated in the corresponding images. PLGA, Poly(lactic-co-glycolic acid); SEM, scanning electron microscopy; XPS, X-ray photoelectron spectroscopy; FT-IR, Fourier-transform infrared spectroscopy.

ear at 0.4%–2.6% strain, yielding a compressive Young's modulus of 4.35 MPa (It is the slope value of the stress-strain curve corresponding to this strain range). At approximately 5% strain, the scaffold reached a yield point with a compressive strength of about 0.27 MPa, after which stress growth slowed and entered a pore-collapse plateau (Fig. 2C). HPLC calibration curves for doxycycline and lactoferrin showed excellent linearity (R^2 > 0.99). Their encapsulation efficiencies were approximately 75% and 55%, with drug-loading capacities of 7.5% and 5.6%, respectively (**Supplementary Table 4**, Fig. 2D,E). Over 240 h, cumulative release reached 88.4% for doxycycline and nearly 60% for lactoferrin. Doxycycline release best fit the Ritger-Peppas model (R^2 = 0.9995, n = 0.45), whereas lactoferrin fit both Ritger-Peppas and Higuchi models well (R^2 = 0.9991 and 0.9978), supporting sustained diffusion-dominated release without an obvious burst effect (Fig. 2F,G). These properties collectively support effective drug incorporation and prolonged release from the porous scaffold.

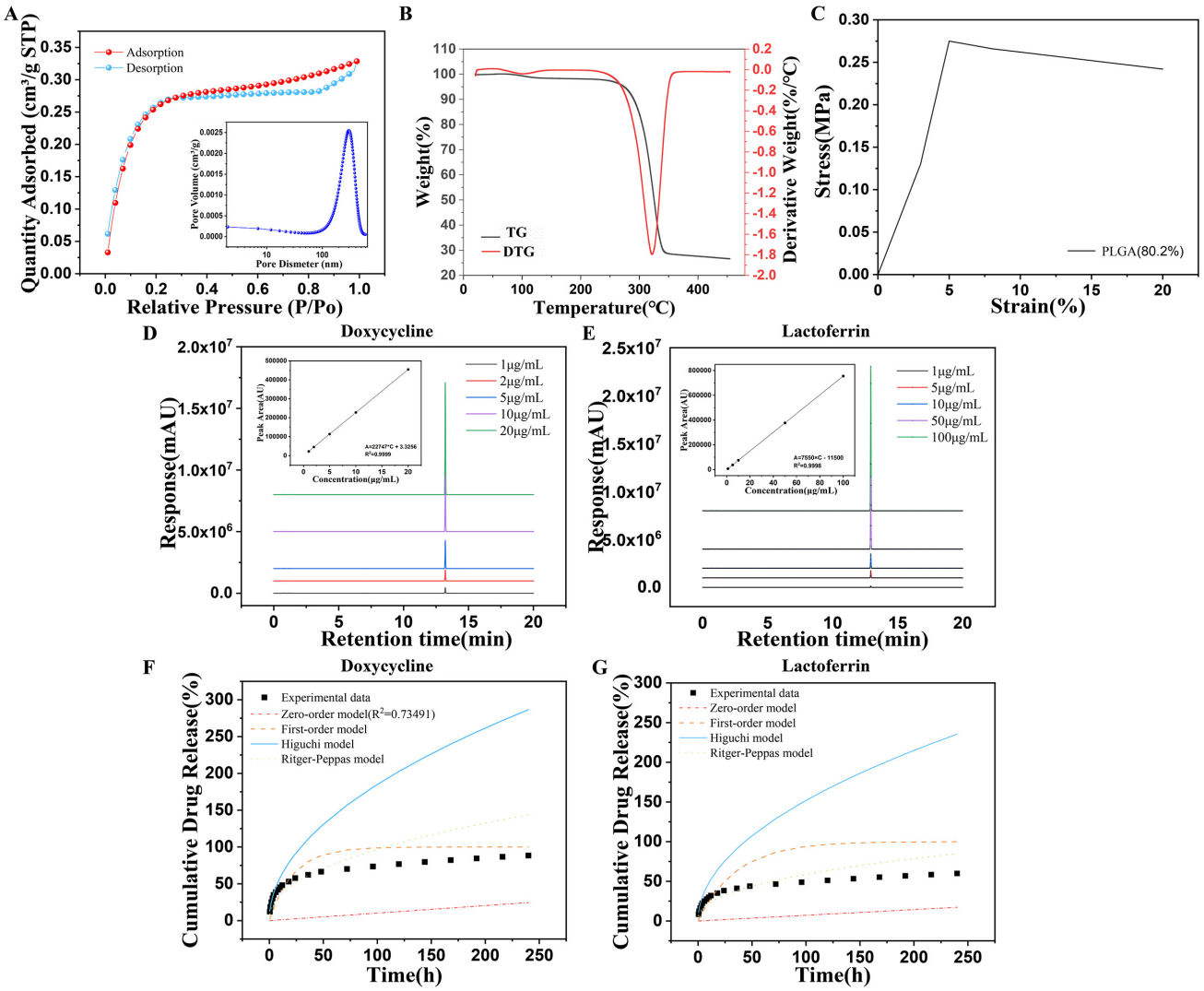

Fig. 2. Physicochemical properties and *in vitro* dual-drug release from the PLGA/DOX-LF scaffold. (A) Nitrogen adsorption-desorption isotherm; the inset shows the BJH pore-size distribution. (B) TG and DTG curves describing thermal degradation. (C) Representative compressive stress-strain curve. (D,E) HPLC chromatograms of doxycycline and lactoferrin standards at different concentrations, with the corresponding calibration curves shown in the insets. (F,G) Cumulative release profiles of doxycycline and lactoferrin over 240 h and fitting using zero-order, first-order, Higuchi, and Ritger-Peppas kinetic models. n = 3 independent replicates. DOX, doxycycline hydrochloride; LF, lactoferrin; BJH, Barrett-Joyner-Halenda; TG, thermogravimetric; DTG, derivative thermogravimetric.

Live/dead staining showed abundant viable bacteria and only sparse dead bacteria in the Control and blank PLGA groups, with no significant difference between them (Fig. 3). PLGA/DOX markedly reduced the live-bacterial signal and increased dead-bacterial fluorescence, decreasing relative bacterial viability to approximately 30% ($p < 0.001$). PLGA/LF produced a moderate reduction to approximately 70% ($p < 0.05$), indicating measurable antibacterial activity of LF alone. The PLGA/DOX-LF scaffold yielded the lowest live-bacterial abundance and the strongest dead-bacterial signal, reducing viability to approximately 20% ($p < 0.001$) and demonstrating the most pronounced overall antibacterial effect.

3.2 Regulatory Effect of PLGA/DOX-LF on Macrophage Polarization

To evaluate the immunomodulatory effects of the scaffold formulations, RAW264.7 macrophages were exposed to extracts from blank PLGA, PLGA/DOX, PLGA/LF, or PLGA/DOX-LF scaffolds. CCK-8 analysis showed no significant differences in cell viability among the groups, confirming that neither the unloaded scaffold nor the single- or dual-drug-loaded formulations caused detectable cytotoxicity (Fig. 4A). Under *P.g.*-LPS stimulation, macrophages displayed a pronounced M1-like phenotype, characterized by increased CD86 fluorescence and reduced CD206 fluorescence relative to untreated controls ($p < 0.001$). Blank PLGA did not significantly alter this response. In contrast,

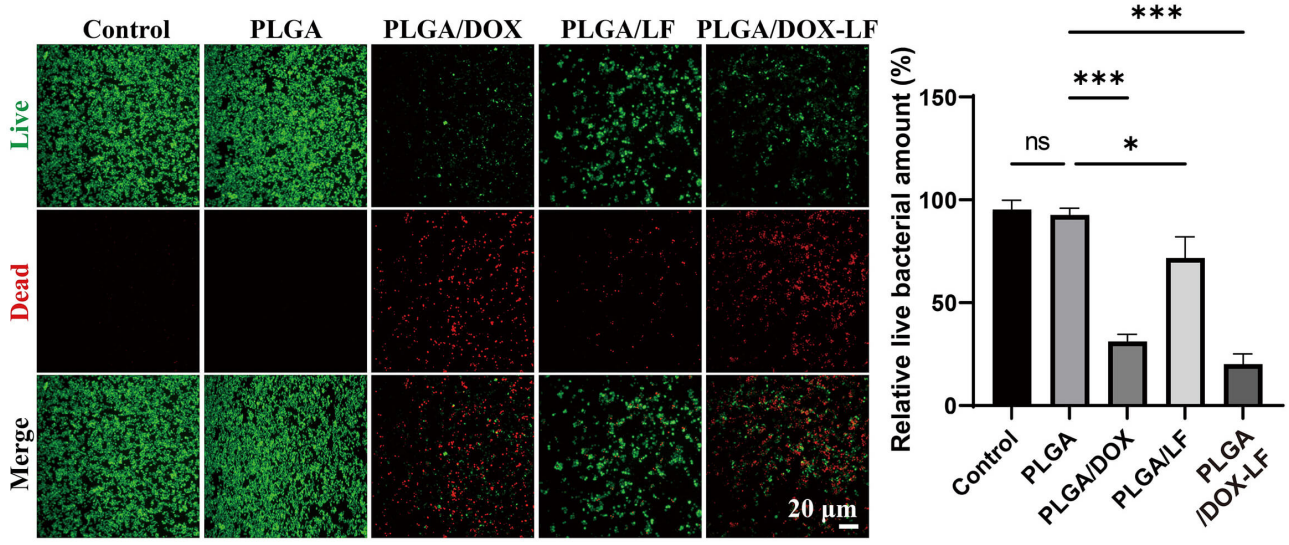

Fig. 3. Antibacterial activity of PLGA-based scaffolds evaluated by bacterial live/dead staining. Bacteria were treated with Control, blank PLGA, PLGA/DOX, PLGA/LF, or PLGA/DOX-LF scaffolds. Viable and dead bacteria are shown in green and red, respectively, and merged images are presented in the bottom row. The bar graph shows the relative abundance of viable bacteria normalized to the Control group. Data are presented as mean ± SD (n = 3). Scale bar, 20 μm. ns, not significant; *$p < 0.05$; ***$p < 0.001$.

PLGA/DOX and PLGA/LF partially attenuated CD86 expression and restored CD206 expression, with PLGA/LF showing a somewhat stronger M2-promoting effect. The PLGA/DOX-LF scaffold produced the most marked phenotypic shift, reducing CD86 fluorescence to near-baseline levels while increasing CD206 fluorescence above that observed with either single-loaded scaffold (Fig. 4B–D).

RT-qPCR findings were consistent with the immunofluorescence results. LPS markedly increased the expression of the M1-associated genes *iNOS*, *IL-1β*, and *TNF-α*, whereas blank PLGA produced no significant change. Both PLGA/DOX and PLGA/LF significantly reduced these pro-inflammatory transcripts, and the dual-loaded PLGA/DOX-LF scaffold achieved the greatest suppression (Fig. 4E). Conversely, LPS decreased the M2-associated markers *CD206*, *Arg-1*, and *IL-10*. Single-drug scaffolds partially restored their expression, while PLGA/DOX-LF induced the strongest upregulation, particularly for *Arg-1* and *IL-10* (Fig. 4F). The superiority of the dual-loaded formulation over the corresponding single-drug groups was statistically supported across most polarization indices. These results indicate that the PLGA/DOX-LF composite scaffold can effectively inhibit macrophage polarization towards the M1 phenotype and promote its polarization towards the M2 phenotype, thereby shifting the inflammatory microenvironment towards a state conducive to tissue repair.

3.3 Effect of PLGA/DOX-LF-Regulated Macrophage Polarization on PDLSC Migration and Osteogenic Differentiation

To determine whether PLGA/DOX-LF-mediated macrophage reprogramming influenced periodontal regeneration, PDLSCs were exposed either directly to scaffold extracts or to CM collected from differently treated RAW264.7 macrophages. Direct exposure to blank PLGA or PLGA/DOX-LF extracts did not significantly affect PDLSC viability, and Calcein-AM/PI staining revealed abundant viable cells with only sporadic dead cells, confirming the favorable cytocompatibility of the scaffolds (Fig. 5A,B). In contrast, CM from LPS-stimulated macrophages markedly reduced PDLSC viability relative to the untreated control ($p < 0.001$), whereas blank PLGA did not alleviate this inhibitory effect. CM derived from the PLGA/DOX- and PLGA/LF-treated macrophages partially restored cell viability, while PLGA/DOX-LF-associated CM produced the greatest recovery, approaching the control level (Fig. 5C).

Transwell assays further demonstrated that inflammatory CM substantially impaired PDLSC migration. The migration rate remained comparably low in the LPS and LPS + PLGA groups, whereas CM from the LPS + PLGA/DOX-LF group significantly increased migration to approximately 70% of the control value ($p < 0.001$; Fig. 5D,E). Consistent with these findings, LPS-conditioned CM markedly suppressed early osteogenic differentiation, as indicated by weak ALP staining and reduced ALP activity. Blank PLGA exerted no significant protective effect, whereas PLGA/DOX-LF-associated CM restored ALP activity to approximately 70%–75% of the control level (Fig.

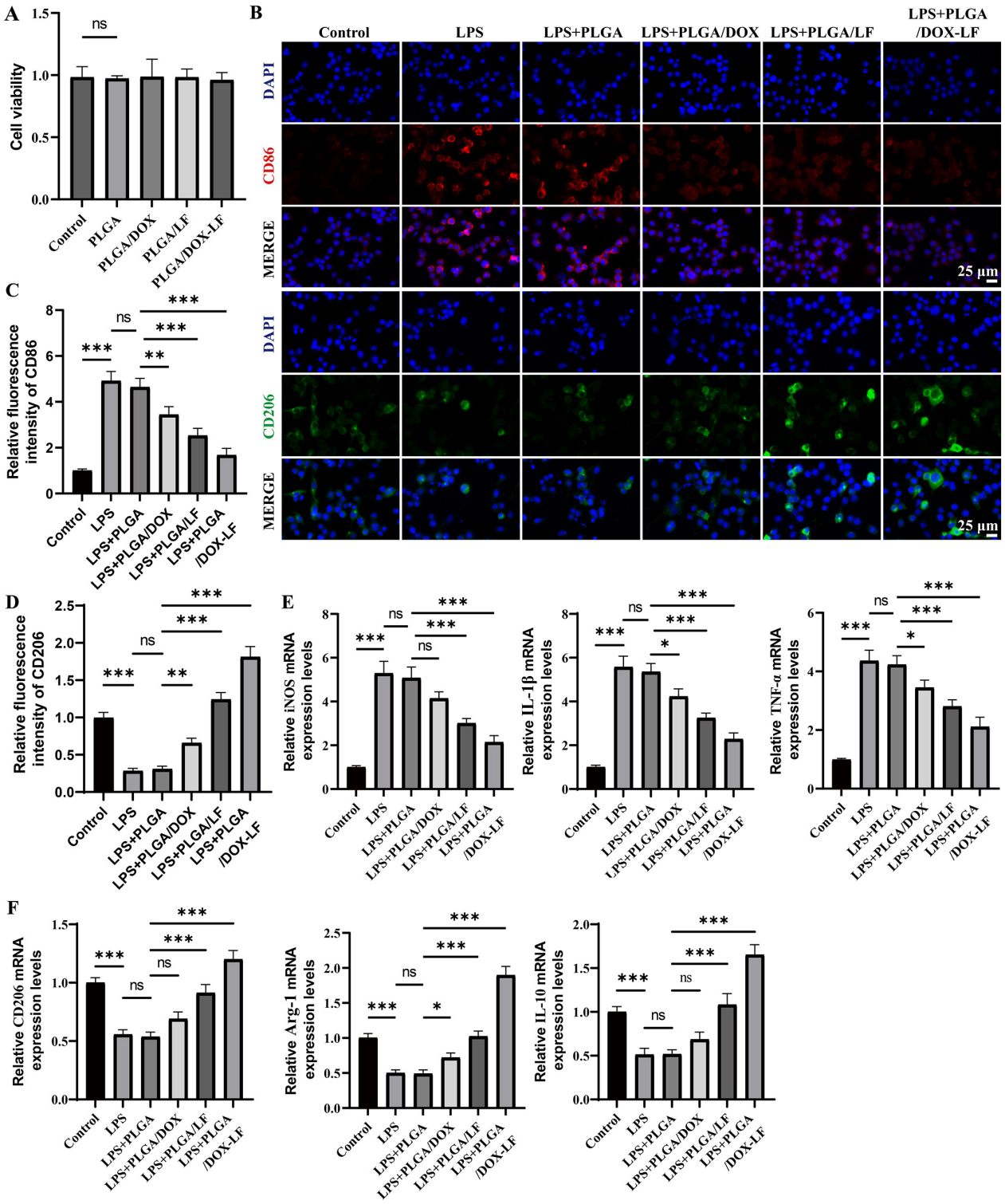

Fig. 4. Effects of PLGA-based scaffold formulations on RAW264.7 macrophage viability and polarization. (A) CCK-8 assay of cells treated with extracts from blank PLGA, PLGA/DOX, PLGA/LF, or PLGA/DOX-LF scaffolds (n = 6). (B) Representative immunofluorescence images of CD86 (red), CD206 (green), and DAPI-stained nuclei (blue) after LPS stimulation and scaffold treatment (n = 3). Scale bars: 25 μm. (C,D) Quantification of CD86 and CD206 fluorescence intensities. (E) Relative mRNA expression of the M1-associated genes *iNOS*, *IL-1β*, and *TNF-α* (n = 6). (F) Relative mRNA expression of the M2-associated genes *CD206*, *Arg-1*, and *IL-10* (n = 6). Data are presented as mean ± SD. ns, not significant; *$p < 0.05$; **$p < 0.01$; ***$p < 0.001$. CCK-8, Cell Counting Kit-8; CD86, cluster of differentiation 86 CD206, cluster of differentiation 206; LPS, lipopolysaccharide; iNOS, inducible nitric oxide synthase; Arg-1, arginase-1.

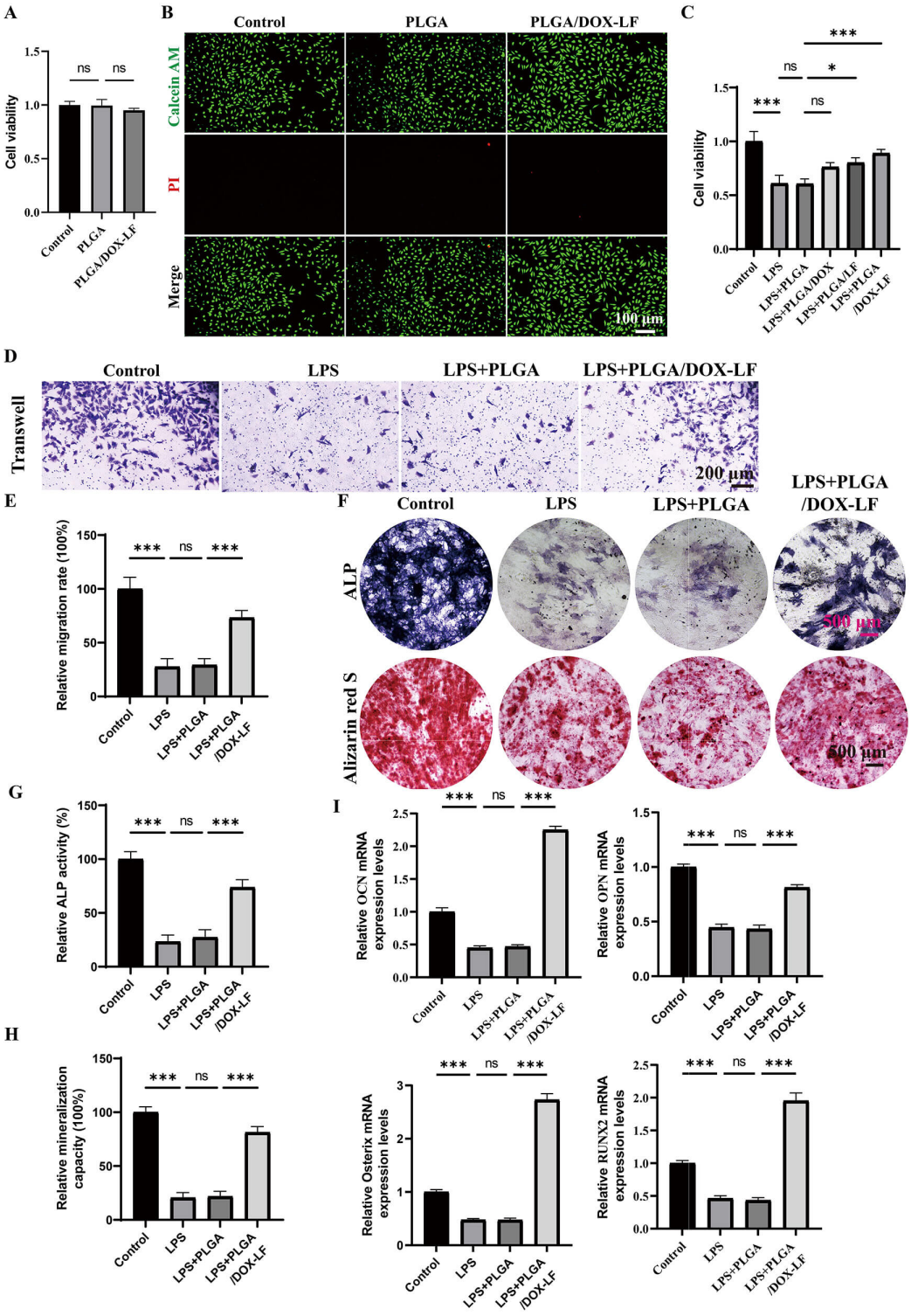

Fig. 5. Effects of PLGA/DOX-LF-regulated macrophage-conditioned medium on PDLSC viability, migration, and osteogenic differentiation. (A,B) CCK-8 assay and Calcein-AM/PI staining of PDLSCs directly exposed to scaffold extracts (n = 3). Scale bar, 100 μm. (C) Viability of PDLSCs cultured with conditioned media from differently treated macrophages (n = 6). (D,E) Representative Transwell images and quantitative migration rates (n = 3). Scale bar: 200 μm. (F) Representative ALP and Alizarin Red S staining after osteogenic induction. Scale bars, 500 μm. (G,H) Quantification of ALP activity and mineralization capacity. (I) Relative mRNA expression of *OCN*, *OPN*, *Osterix*, and *RUNX2* (n = 6). Data are mean ± SD. ns, not significant; *$p < 0.05$; ***$p < 0.001$. PDLSCs, periodontal ligament stem cells; Calcein-AM/PI, Calcein-acetoxymethyl ester/propidium iodide; ALP, alkaline phosphatase; OCN, osteocalcin; OPN, osteopontin; RUNX2, Runt-related transcription factor 2.

5F,G). Alizarin Red S staining showed a similar pattern: mineralized nodule formation was markedly reduced by LPS and remained low after blank PLGA treatment, but was substantially restored by PLGA/DOX-LF-associated CM, reaching approximately 80% of the control mineralization capacity (Fig. 5F,H).

RT-qPCR analysis corroborated the staining results. LPS significantly downregulated osteocalcin (*OCN*), osteopontin (*OPN*), Osterix (*Osterix*), and Runt-related transcription factor 2 (*RUNX2*), whereas blank PLGA caused no significant improvement. PLGA/DOX-LF-associated CM markedly increased all four osteogenic transcripts, with OCN, Osterix, and RUNX2 reaching or exceeding control levels (Fig. 5I). These results demonstrate that PLGA/DOX-LF-induced macrophage modulation creates a pro-regenerative paracrine environment that supports PDLSC survival, migration, matrix mineralization, and osteogenic differentiation.

3.4 Effect of PLGA/DOX-LF-Regulated Macrophage Polarization on Angiogenesis

To determine whether PLGA/DOX-LF-mediated macrophage reprogramming enhanced angiogenesis, HUVECs were treated either directly with scaffold extracts or with CM from differently treated macrophages. Direct exposure to blank PLGA or PLGA/DOX-LF extracts did not significantly affect HUVEC viability, confirming good endothelial cytocompatibility (Fig. 6A). In contrast, CM from LPS-stimulated macrophages markedly reduced HUVEC viability compared with the Control group ($p < 0.001$), whereas blank PLGA produced no significant improvement. CM associated with the single-drug scaffolds partially restored viability, while PLGA/DOX-LF-associated CM elicited the greatest recovery (Fig. 6B).

Tube-formation assays showed that LPS-conditioned CM substantially disrupted vascular network formation, as evidenced by sparse and discontinuous tubular structures and a pronounced reduction in total tube length. Blank PLGA did not alleviate this impairment, whereas PLGA/DOX-LF-associated CM significantly restored the formation of dense, interconnected capillary-like networks and increased total tube length ($p < 0.01$; Fig. 6C,D). Consistently, PLGA/DOX-LF-associated CM markedly upregulated the angiogenesis-related genes cluster of differentiation 31 (*CD31*), platelet-derived growth factor subunit BB (*PDGF-BB*), matrix metalloproteinase 9 (*MMP9*), and vascular endothelial growth factor A (*VEGF-A*) compared with the LPS + PLGA group (all $p < 0.001$; Fig. 6E). These findings indicate that PLGA/DOX-LF-mediated macrophage modulation establishes a pro-angiogenic paracrine microenvironment that supports endothelial survival and vascular network formation.

3.5 PLGA/DOX-LF Promotes Macrophage M2 Polarization Partly Through MFGE8 Upregulation

To investigate the molecular mechanism underlying PLGA/DOX-LF-mediated macrophage polarization, MFGE8 expression was assessed at both the transcriptional and protein levels. LPS stimulation significantly decreased *MFGE8* mRNA and protein expression compared with the untreated Control group, whereas blank PLGA produced no significant improvement. PLGA/DOX and PLGA/LF partially restored MFGE8 expression, with a more pronounced effect observed for PLGA/LF. Notably, the dual-loaded PLGA/DOX-LF scaffold induced the highest *MFGE8* mRNA and protein levels, significantly exceeding those observed with either single-drug formulation (Fig. 7A,B).

The functional involvement of MFGE8 was subsequently examined using siRNA-mediated knockdown. RT-qPCR confirmed that si-MFGE8 markedly reduced *MFGE8* expression relative to si-NC ($p < 0.001$; Fig. 7C). Under LPS stimulation, MFGE8 silencing intensified the pro-inflammatory macrophage phenotype, as evidenced by increased CD86 fluorescence and reduced CD206 fluorescence. Addition of the PLGA/DOX-LF scaffold partially reversed these changes, significantly decreasing CD86 expression and restoring CD206 expression despite MFGE8 knockdown (Fig. 7D–F).

RT-qPCR analysis further showed that MFGE8 silencing increased the M1-associated genes *iNOS* and *TNF-α* while suppressing the M2-associated genes *Arg-1* and *IL-10*. PLGA/DOX-LF treatment significantly counteracted these alterations, reducing *iNOS* and *TNF-α* expression and markedly enhancing *Arg-1* and *IL-10* expression (Fig. 7G). Collectively, these results indicate that PLGA/DOX-LF upregulates MFGE8 and thereby contributes to the suppression of M1 polarization and promotion of an M2-like reparative phenotype.

4. Discussion

In this study, we successfully developed a 3D-printed biphasic PLGA composite scaffold, designated PLGA/DOX-LF. *In vitro* findings demonstrated that the scaffold reduced bacterial viability, promoted MFGE8-associated polarization of macrophages toward an M2-like reparative phenotype, and established a paracrine microenvironment favorable for PDLSC osteogenic differentiation and HUVEC angiogenesis, thereby integrating antibacterial activity, immunomodulation, and osteogenic–angiogenic coupling.

4.1 Physicochemical Properties of the Scaffold and the Basis for Immune Regulation

Three-dimensional printing enables precise control over scaffold geometry, pore interconnectivity, and surface architecture, all of which influence macrophage adhesion and polarization. Large-pore 3D-printed PEEK

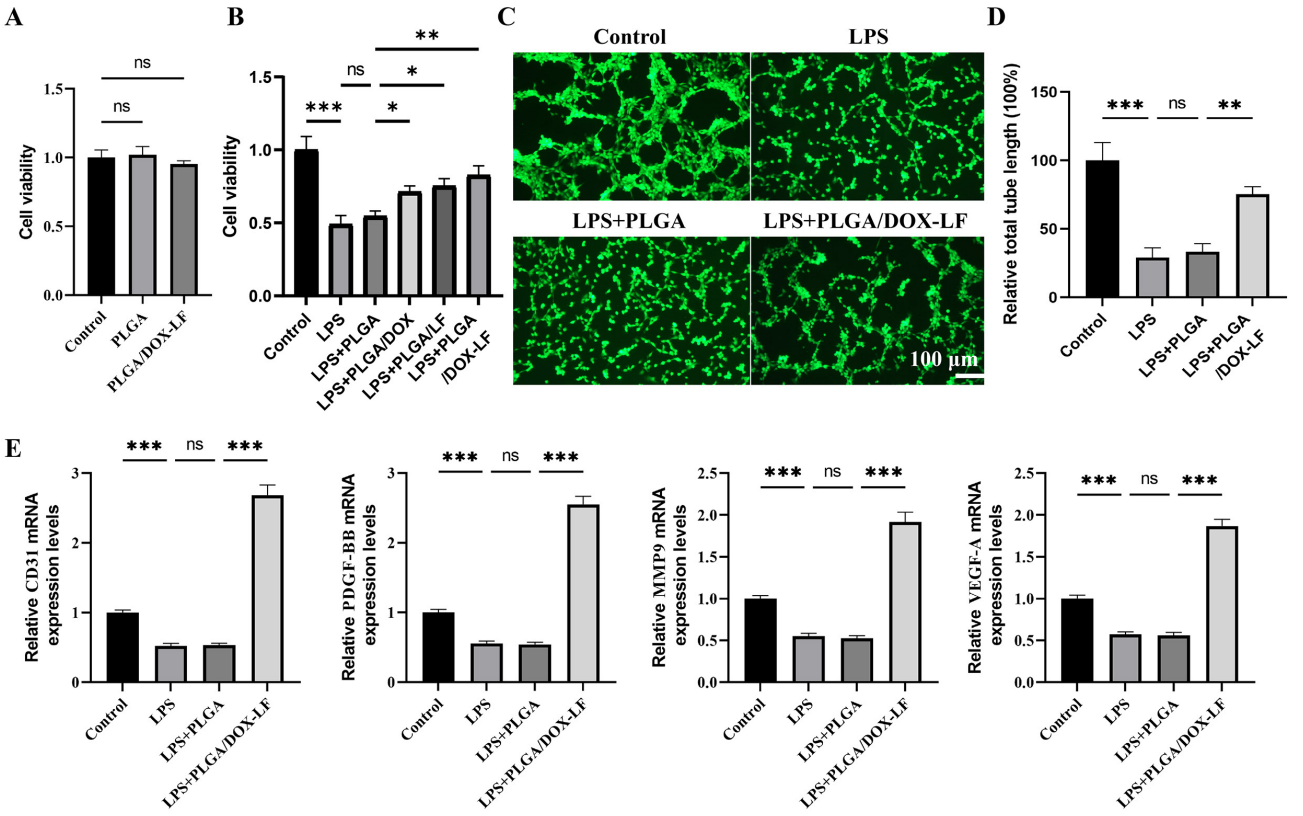

Fig. 6. Effects of PLGA/DOX-LF-regulated macrophage-conditioned medium on HUVEC viability and angiogenesis. (A) HUVEC viability following direct exposure to scaffold extracts (n = 6). (B) Viability of HUVECs cultured with CM from differently treated macrophages (n = 6). (C,D) Representative tube-formation images and quantitative analysis of total branch length (n = 3). Scale bar, 100 μm. (E) Relative mRNA expression of *CD31*, *PDGF-BB*, *MMP9*, and *VEGF-A* (n = 6). Data are presented as mean ± SD. ns, not significant; **p* < 0.05; ***p* < 0.01; ****p* < 0.001. HUVECs, human umbilical vein endothelial cells; CM, conditioned medium; CD31, cluster of differentiation 31; PDGF-BB, platelet-derived growth factor subunit BB; MMP9, matrix metalloproteinase 9; VEGF-A, vascular endothelial growth factor A.

scaffolds have been reported to facilitate the transition from an M1-like to an M2-like phenotype and enhance anti-inflammatory mediator secretion [17]. Similarly, SF/nano-HA-functionalized porous PEEK scaffolds promote M2 polarization through integrin β1-dependent interactions and calcium-sensing receptor signaling [30]. PLGA offers favorable biocompatibility, controllable degradation, and adaptable drug-release properties. When combined with a biphasic architecture integrating microspheres and nanoscale carriers, it may support staged or sustained delivery of bioactive components. Consistent with this concept, SPION/PLGA magnetic scaffolds and PLGA/Fe_2O_3 composites enhance M2-associated responses, partly through PI3K/AKT-related signaling [21,31]. Similarly, a PLGA/DBM-MPs/MH-NPs scaffold was reported to create a stage-matched osteogenic microenvironment by modulating early osteo-immunomodulation, middle neovascularization, and later osteogenesis [32]. In the present system, structural cues together with DOX, LF, FGF2, and BMP9 may jointly contribute to antibacterial activity, immunomodulation, angiogenesis, and bone regeneration. Although the material compositions differ, both strategies integrate immunomodulatory and regenerative functions within PLGA-based scaffolds, while the present design additionally enables localized delivery of multiple bioactive agents.

4.2 The Core Mechanism of MFGE8-Mediated Macrophage M2 Polarization

Our findings indicate that MFGE8 contributes substantially, although not exclusively, to PLGA/DOX-LF-mediated macrophage reprogramming. MFGE8 is a secreted bridging protein that links phosphatidylserine on apoptotic cells to integrins on phagocytes, thereby promoting efferocytosis and inflammation resolution. In bone-injury settings, MFGE8 has been associated with M2b polarization and reduced fibrotic deposition through signal transducer and activator of transcription 3 (STAT3)/arginase-1 (Arg1)-related signaling [33]. In tumor-associated macrophages, MFGE8-mediated recognition of apoptotic cells likewise favors an M2-like phenotype [34]. Mechanistically, MFGE8 can engage αvβ3 integrin

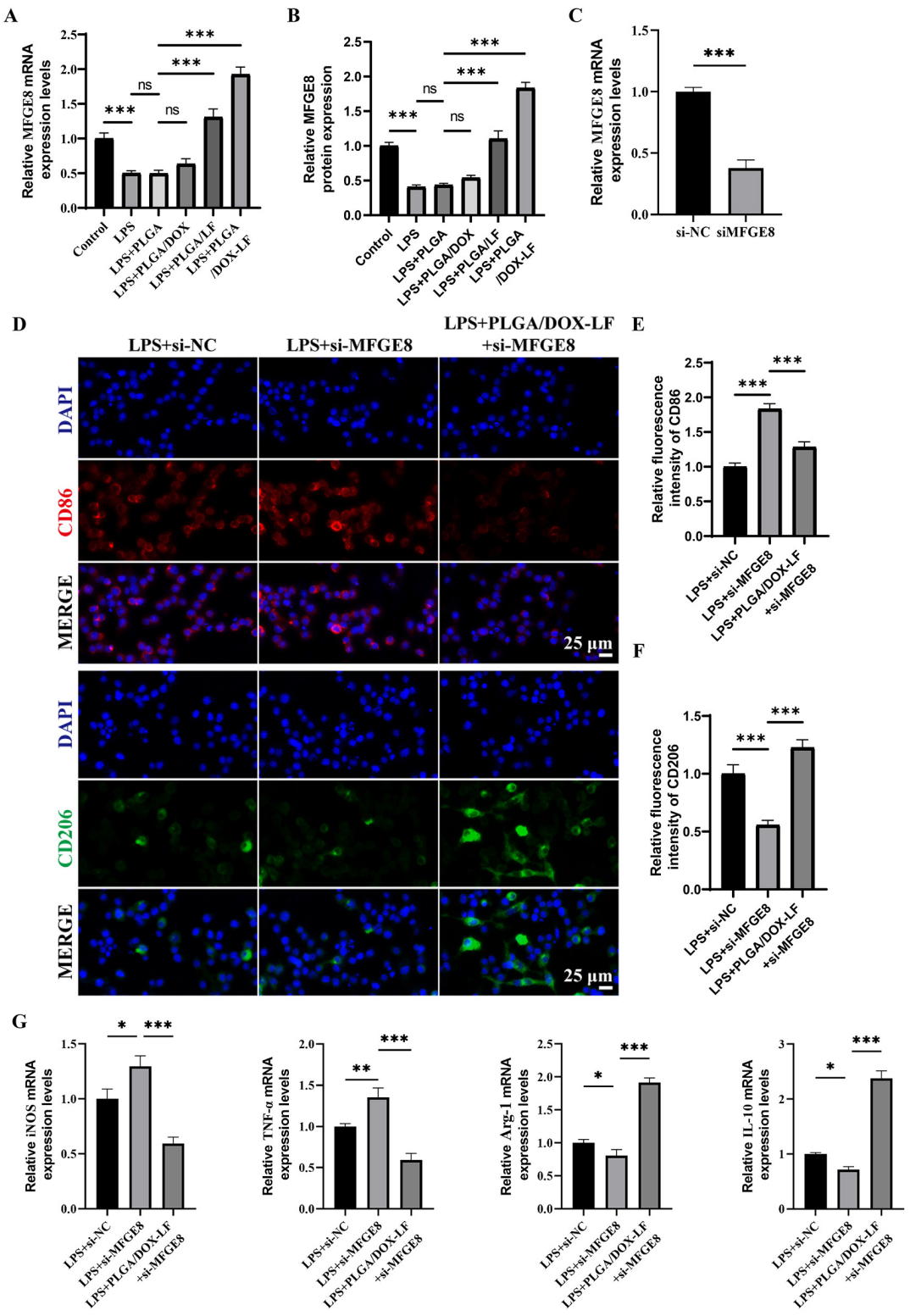

Fig. 7. Involvement of MFGE8 in PLGA/DOX-LF-mediated macrophage polarization. (A,B) *MFGE8* mRNA and protein levels determined by RT-qPCR and ELISA, respectively (n = 6). (C) Validation of siRNA-mediated *MFGE8* knockdown (n = 3). (D) Representative immunofluorescence images of CD86 and CD206 after MFGE8 silencing and PLGA/DOX-LF treatment (n = 3). Scale bars: 25 μm. (E,F) Quantification of CD86 and CD206 fluorescence intensities. (G) Relative expression of *iNOS*, *TNF-α*, *Arg-1*, and *IL-10* (n = 6). Data are mean ± SD. ns, not significant; *$p < 0.05$; **$p < 0.01$; ***$p < 0.001$. MFGE8, milk fat globule-epidermal growth factor 8; RT-qPCR, reverse transcription-quantitative polymerase chain reaction.

and activate Src-focal adhesion kinase (FAK)-STAT3 signaling, supporting the MFGE8/STAT3/Arg1 axis [33,35]. Conversely, impaired MFGE8-dependent apoptotic-cell clearance has been linked to defective inflammation resolution [36]. In our study, the scaffold increased MFGE8 expression, whereas siRNA-mediated knockdown intensified M1-associated responses and weakened M2-associated markers. Because PLGA/DOX-LF partially retained activity after MFGE8 silencing, additional pathways are likely involved. NLRP3-associated signaling may represent one such pathway, given its relationship with M1 polarization in lipopolysaccharide-treated periodontal ligament stem cell-derived extracellular vesicle (L-PDLSC-EV) studies [37], but this possibility requires direct experimental verification.

4.3 Regulatory Role of M2-Polarized Macrophages in Multicellular Synergistic Regeneration

M2-like macrophages can establish a regenerative paracrine environment coordinating stem-cell activity, vascularization, and bone remodeling [38]. In this study, conditioned medium from PLGA/DOX-LF-treated macrophages improved PDLSC migration, ALP activity, mineralized nodule formation, and osteogenic gene expression, indicating that immune modulation indirectly enhanced periodontal progenitor-cell function. This interpretation agrees with reports showing that M2-favoring conditions increase PDLSC osteogenic potential; for example, low-dose tumor necrosis factor-like weak inducer of apoptosis (TWEAK) promotes M2 polarization and PDLSC osteogenesis through fibroblast growth factor-inducible 14 (Fn14)/NF-κB signaling [39]. M2-derived mediators, including VEGF and BMP-2, can also stimulate endothelial tube formation through PI3K/AKT/HIF-1α-related pathways [40,41]. Likewise, conditioned medium from three-dimensional printed-electrospun fibrous (3D-M-EF) scaffolds enhances osteogenic differentiation and vascularized bone formation [40], whereas poly-L-lactic acid/manganese dioxide (PLLA/MnO_2) scaffolds coordinate osteogenesis and angiogenesis through transforming growth factor-beta (TGF-β)/Smad signaling [42]. M2 macrophages may additionally restrain osteoclast activity through IL-10 and TGF-β, shifting the local balance from resorption toward regeneration. Evidence from B10-cell-mediated regulation of macrophage polarization in periodontitis further supports this concept [43]. Collectively, these findings reinforce a scaffold-macrophage - osteogenesis/angiogenesis axis that may generate a positive feedback loop between immunomodulation and tissue repair [44].

Recent immunomodulatory periodontal constructs include 1,2,3-triazole-phosphine oxide grafted (TPG)-functionalized PLGA/PCL electrospun membranes, which suppress PI3K/AKT and NF-κB signaling and promote periodontal regeneration in rats, and infection-sensitive SPION/PLGA scaffolds, which combine bacterial anti-adhesion with NLRP3 downregulation and IL-10-associated M2 polarization [21,45]. More recently, M2 macrophage-loaded hybrid scaffolds enhanced cell homing, angiogenesis, and early periodontal osteogenesis [46]. Compared with these systems, our acellular 3D-printed PLGA/DOX-LF scaffold integrates sustained local antibacterial delivery with MFGE8-associated macrophage reprogramming and downstream osteogenic-angiogenic coupling. Its cell-free formulation may facilitate storage and implantation relative to cell-loaded constructs. However, unlike the aforementioned platforms that have undergone *in vivo* evaluation, the present evidence remains predominantly *in vitro*; periodontal defect models and head-to-head comparisons are therefore required to establish relative efficacy, degradation behavior, and long-term safety.

4.4 Clinical Translation Potential and Prospects for Multidisciplinary Integration

The proposed strategy aligns with the emerging concept of immune-guided regeneration. Its principal translational advantage lies in combining local antibacterial activity, sustained bioactive-factor delivery, and macrophage-directed immunomodulation within a cell-free 3D-printed scaffold. In principle, this platform could support early suppression of excessive M1-like inflammation, intermediate promotion of M2-associated angiogenesis, and later enhancement of osteogenic remodeling [42,47,48]. Integration with exosome delivery, sequential dual-factor release, or stimuli-responsive materials may further improve temporal control and therapeutic efficiency [49,50,51]. Related immunoregenerative mechanisms have shown efficacy in rabbit osteonecrosis and calvarial-defect models [52,53], providing a rationale for extension to periodontal and maxillofacial repair.

From a translational perspective, oral inflammatory biomarkers evolve dynamically with disease activity and therapeutic response. Salivary and peri-implant crevicular fluid IL-1β, MMP-8, and MMP-9 are generally elevated in periodontitis or peri-implantitis, whereas effective treatment may reduce MMP-8, TNF-α, and related inflammatory mediators [54,55,56]. Thus, the decreased iNOS, TNF-α, IL-1β, and CD86 levels, together with increased Arg-1, IL-10, CD206, MFGE8, osteogenic, and angiogenic markers observed here, may reflect a transition from tissue-destructive inflammation toward resolution and regeneration. Future studies should longitudinally validate these biomarker trajectories in saliva and crevicular fluid to establish clinically applicable response panels.

4.5 Limitations

This study successfully constructed a 3D-printed PLGA biphasic composite scaffold loaded with DOX and LF, confirming that it induces macrophage M2 polarization by upregulating MFGE8, thereby creating a regenerative microenvironment that couples osteogenesis and angiogenesis. However, this study has some limitations. First,

the findings were derived primarily from *in vitro* monoculture and macrophage-conditioned-medium systems; therefore, the regenerative efficacy, biodegradation behavior, mechanical stability, and long-term biosafety of the scaffold require validation in periodontal defect models. Second, the antibacterial assessment was short-term and limited to a single bacterial species, which does not fully reproduce the polymicrobial biofilm environment of periodontitis. Third, although MFGE8 knockdown attenuated the immunomodulatory effects of PLGA/DOX-LF, rescue or overexpression experiments and downstream pathway analyses were not performed, preventing definitive establishment of the complete causal mechanism. In addition, the release study covered only 240 h, whereas periodontal regeneration occurs over a substantially longer period. Future studies should optimize the spatiotemporal release of DOX and LF and evaluate the scaffold in clinically relevant animal models.

5. Conclusions

The 3D-printed biphasic PLGA scaffold achieved sustained local drug delivery, reduced *P. gingivalis* viability, and shifted LPS-stimulated macrophages toward an MFGE8-associated M2-like phenotype. Macrophage-conditioned medium subsequently improved PDLSC migration, osteogenic differentiation, and HUVEC angiogenic activity, supporting coordinated immunomodulatory and regenerative effects. MFGE8 knockdown attenuated, but did not completely abolish, these responses, indicating that additional pathways may contribute. Collectively, the findings establish an *in vitro* proof of concept for this multifunctional scaffold as a candidate platform for inflammatory periodontal regeneration. Its therapeutic efficacy, degradation behavior, release coordination, and long-term safety must be confirmed in polymicrobial and periodontal-defect animal models.

Availability of Data and Materials

The raw data supporting the conclusions of this article will be made available by the authors, without undue reservation.

Author Contributions

YPH: Data curation, Supervision, Investigation, Writing. CFW, CJW: Investigation, Data curation, Methodology, Writing. CX: Data curation, Validation, Writing – review and editing. All authors contributed to editorial changes in the manuscript. All authors read and approved the final manuscript. All authors have participated sufficiently in the work and agreed to be accountable for all aspects of the work.

Ethics Approval and Consent to Participate

Not applicable.

Acknowledgment

The authors gratefully acknowledge the Hunan University of Medicine and the Eighth Affiliated Hospital, Southern Medical University for providing laboratory facilities and technical support. The graphical abstract was created using Figdraw 2.0 and further optimized with Adobe Illustrator 2023.

Funding

Hunan Provincial Natural Science Foundation Regional Joint Project: Research on the Repair of Inflammatory Periodontal Tissue Defects by 3D Printing PLGA Biphase Composite Scaffold Materials Loaded with DOX-LF and Its Mechanism (No. 2025JJ70419).

Conflicts of Interest

The authors declare no conflicts of interest.

Supplementary Material

Supplementary material associated with this article can be found, in the online version, at https://doi.org/10.31083/FBL54017.

References

[1] Jeon HH, Huang X, Rojas Cortez L, Sripinun P, Lee JM, Hong JJ, et al. Inflammation and mechanical force-induced bone remodeling. Periodontology 2000. 2024. https://doi.org/10.1111/prd.12619 (online ahead of print)

[2] Bhuyan R, Bhuyan SK, Mohanty JN, Das S, Juliana N, Juliana IF. Periodontitis and Its Inflammatory Changes Linked to Various Systemic Diseases: A Review of Its Underlying Mechanisms. Biomedicines. 2022; 10: 2659. https://doi.org/10.3390/biomedicines10102659

[3] Duran-Pinedo A, Solbiati J, Teles F, Teles R, Zang Y, Frias-Lopez J. Long-term dynamics of the human oral microbiome during clinical disease progression. BMC Biology. 2021; 19: 240. https://doi.org/10.1186/s12915-021-01169-z

[4] de Campos Kajimoto N, de Paiva Buischi Y, Mohamadzadeh M, Loomer P. The Oral Microbiome of Peri-Implant Health and Disease: A Narrative Review. Dentistry Journal. 2024; 12: 299. https://doi.org/10.3390/dj12100299

[5] Dutra TP, Robitaille N, Altabtbaei K, Dabdoub SM, Kumar PS. Community dynamics during de novo colonization of the nascent peri-implant sulcus. International Journal of Oral Science. 2025; 17: 37. https://doi.org/10.1038/s41368-025-00367-7

[6] Zeng X, Feng M, Lu J, Wang R, Deng L, Yang Y, et al. Beyond transcription, aryl hydrocarbon receptor plays a protective role in periodontitis by interacting with CaMKII. Journal of Periodontology. 2025; 96: 67–81. https://doi.org/10.1002/JPER.24-0021

[7] Ding T, Kang W, Li J, Yu L, Ge S. An in situ tissue engineering scaffold with growth factors combining angiogenesis and osteoimmunomodulatory functions for advanced periodontal bone regeneration. Journal of Nanobiotechnology. 2021; 19: 247. https://doi.org/10.1186/s12951-021-00992-4

[8] Qiao D, Cheng S, Song S, Zhang W, Chen B, Yan F, et al. Polarized M2 macrophages induced by glycosylated nano-hydroxyapatites activate bone regeneration in periodontitis ther-

apy. Journal of Clinical Periodontology. 2024; 51: 1054–1065. https://doi.org/10.1111/jcpe.13999

[9] Peng S, Fu H, Li R, Li H, Wang S, Li B, et al. A new direction in periodontitis treatment: biomaterial-mediated macrophage immunotherapy. Journal of Nanobiotechnology. 2024; 22: 359. https://doi.org/10.1186/s12951-024-02592-4

[10] Azizan N, Al-Maleki AR, Karajacob AS, Loke MF, Goh JPE, Kallarakkal TG, et al. Oral microbiome profiling of primary oral candidiasis during infection and post-antifungal therapy. Clinical Oral Investigations. 2026; 30: 179. https://doi.org/10.1007/s00784-026-06827-6

[11] Karadayı B, Karaismailoğlu B, Karadayı S, Arslan A, Gözen ED, Özbek T. The uselessness of using salivary microbiota in forensic identification purposes of a person with recent antibiotic use. Legal Medicine (Tokyo, Japan). 2024; 69: 102338. https://doi.org/10.1016/j.legalmed.2023.102338

[12] Van Holm W, Carvalho R, Delanghe L, Eilers T, Zayed N, Mermans F, et al. Antimicrobial potential of known and novel probiotics on in vitro periodontitis biofilms. NPJ Biofilms and Microbiomes. 2023; 9: 3. https://doi.org/10.1038/s41522-023-00370-y

[13] Isola G, Polizzi A, Angjelova A, Jovanova E, Pizzo G, Sculean A. Impact and efficacy of systemic antibiotics for peri-implant diseases treatment: A systematic review and meta-analysis on clinical and microbiological outcomes. Periodontology 2000. 2026. https://doi.org/10.1111/prd.70033 (online ahead of print)

[14] Cui Z, Wang P, Gao W. Microbial dysbiosis in periodontitis and peri-implantitis: pathogenesis, immune responses, and therapeutic. Frontiers in Cellular and Infection Microbiology. 2025; 15: 1517154. https://doi.org/10.3389/fcimb.2025.1517154

[15] Wei X, Qian S, Yang Y, Mo J. Microbiome-based therapies for periodontitis and peri-implantitis. Oral Diseases. 2024; 30: 2838–2857. https://doi.org/10.1111/odi.14782

[16] Puzhankara L, Banerjee A, Chopra A, Venkitachalam R, Kedlaya MN. Effectiveness of probiotics compared to antibiotics to treat periodontal disease: Systematic review. Oral Diseases. 2024; 30: 2820–2837. https://doi.org/10.1111/odi.14781

[17] Yang X, Gao J, Yang S, Wu Y, Liu H, Su D, et al. Pore size-mediated macrophage M1 to M2 transition affects osseointegration of 3D-printed PEEK scaffolds. International Journal of Bioprinting. 2023; 9: 755. https://doi.org/10.18063/ijb.755

[18] Cen C, Zhang Y, Cao Y, Hu C, Tang L, Liu C, et al. Construction of a 3D Degradable PLLA/β-TCP/CS Scaffold for Establishing an Induced Membrane Inspired by the Modified Single-Stage Masquelet Technique. ACS Biomaterials Science & Engineering. 2025; 11: 1629–1645. https://doi.org/10.1021/acsbiomaterials.4c01849

[19] Liu B, Du Y, Wang M, Zhang Z, Yin W, Hu Y, et al. Effects of the Dental Implant Surface Topography and Macrophage Polarisation on Osteogenesis and Angiogenesis. International Dental Journal. 2026; 76: 109398. https://doi.org/10.1016/j.identj.2025.109398

[20] He Z, Liu Y, Zheng ZL, Lv JC, Liu SB, Zhang J, et al. Periodic Lamellae-Based Nanofibers for Precise Immunomodulation to Treat Inflammatory Bone Loss in Periodontitis. Advanced Healthcare Materials. 2024; 13: e2303549. https://doi.org/10.1002/adhm.202303549

[21] Guo Y, Shi Z, Han L, Qin X, You J, Zhang Q, et al. Infection-Sensitive SPION/PLGA Scaffolds Promote Periodontal Regeneration via Antibacterial Activity and Macrophage-Phenotype Modulation. ACS Applied Materials & Interfaces. 2024; 16: 41855–41868. https://doi.org/10.1021/acsami.4c06430

[22] Chen L, Hu P, Hong X, Li B, Ping Y, Chen S, et al. Dimethyl fumarate modulates M1/M2 macrophage polarization to ameliorate periodontal destruction by increasing TUFM-mediated mitophagy. International Journal of Oral Science. 2025; 17: 32. https://doi.org/10.1038/s41368-025-00360-0

[23] Wang Y, Li C, Wan Y, Qi M, Chen Q, Sun Y, et al. Quercetin-Loaded Ceria Nanocomposite Potentiate Dual-Directional Immunoregulation via Macrophage Polarization against Periodontal Inflammation. Small (Weinheim an Der Bergstrasse, Germany). 2021; 17: e2101505. https://doi.org/10.1002/smll.202101505

[24] Zhang X, Liu J, Li Y, Li W, Gu D, Chong YT, et al. Erythropoietin Functionalized Hierarchical Scaffolds Enable Immunomodulated and Vascularized Bone Repair in Periodontal Defect. ACS Applied Materials & Interfaces. 2026; 18: 14256–14273. https://doi.org/10.1021/acsami.5c24484

[25] Zhang Z, Zeng L, Yu Y, Xu Z, Zhu G, Weng J, et al. hPDLSC-ApoEVs attenuate periodontitis and enhance bone regeneration via NF-κB/S100A9-Mediated M2 macrophage polarization. Stem Cell Research & Therapy. 2025; 16: 508. https://doi.org/10.1186/s13287-025-04617-7

[26] Liu Y, Zhao Y, Zhu W, Han M, Mi F, Wang B. Comprehensive reparative effects of bacteriostatic poly(L-lactide-co-glycolide)/poly(L-lactide-co-ε-caprolactone) electrospinning membrane on alveolar bone defects in progressive periodontitis. Journal of Biomedical Materials Research. Part B, Applied Biomaterials. 2023; 111: 513–525. https://doi.org/10.1002/jbm.b.35168

[27] Pedrini F, Nazato VS, Hausen MA, Komatsu D, Peña SS, Almeida ALM, et al. In Vitro Cell Behavior and Antibiotic Activity under Sustained Release of Doxycycline-Loaded Poly(lactic-co-glycolic acid) Microspheres. Antibiotics (Basel, Switzerland). 2022; 11: 945. https://doi.org/10.3390/antibiotics11070945

[28] Kim JW, Lee JS, Choi YJ, Kim C. The Multifaceted Functions of Lactoferrin in Antimicrobial Defense and Inflammation. Biomolecules. 2025; 15: 1174. https://doi.org/10.3390/biom15081174

[29] Kosznik-Kwaśnicka K, Leszczyńska U, Piechowicz L. Lactoferrin bridges antimicrobial and healing responses in *Staphylococcus aureus* skin infections. Frontiers in Microbiology. 2026; 16: 1753483. https://doi.org/10.3389/fmicb.2025.1753483

[30] Zhu M, Hu L, Liu Y, Chen P, Wang X, Tang B, et al. A Surface-Mediated Biomimetic Porous Polyether-Ether-Ketone Scaffold for Regulating Immunity and Promoting Osteogenesis. ACS Biomaterials Science & Engineering. 2024; 10: 6120–6134. https://doi.org/10.1021/acsbiomaterials.4c00725

[31] Liu J, Liu F, Li C, Li Z, Li T, Wu Y, et al. 3D-printed magnetic scaffolds promote bone and vessel regeneration through CRYAB/PI3K-AKT and NF-κB pathways identified by proteomics. Bioactive Materials. 2026; 56: 277–293. https://doi.org/10.1016/j.bioactmat.2025.10.013

[32] Yuan Y, Xu Y, Mao Y, Liu H, Ou M, Lin Z, et al. Three Birds, One Stone: An Osteo-Microenvironment Stage-Regulative Scaffold for Bone Defect Repair through Modulating Early Osteo-Immunomodulation, Middle Neovascularization, and Later Osteogenesis. Advanced Science. 2024; 11: e2306428. https://doi.org/10.1002/advs.202306428

[33] Lai H, Yip HC, Gong Y, Chan KF, Leung KKC, Chan MS, et al. MFGE8 in exosomes derived from mesenchymal stem cells prevents esophageal stricture after endoscopic submucosal dissection in pigs. Journal of Nanobiotechnology. 2024; 22: 143. https://doi.org/10.1186/s12951-024-02429-0

[34] Liu W, Li L, Bai X, Zhang M, Lv W, Ma Y, et al. Osteosarcoma Cell-Derived Migrasomes Promote Macrophage M2 Polarization to Aggravate Osteosarcoma Proliferation and Metastasis. Advanced Science (Weinheim, Baden-Wurttemberg, Germany). 2025; 12: e2409870. https://doi.org/10.1002/advs.202409870

[35] Ma Z, Sun Y, Yu Y, Xiao W, Xiao Z, Zhong T, et al. Extracellular vesicles containing MFGE8 from colorectal can-

cer facilitate macrophage efferocytosis. Cell Communication and Signaling: CCS. 2024; 22: 295. https://doi.org/10.1186/s12964-024-01669-9

[36] Hill AA, Kim M, Zegarra-Ruiz DF, Chang LC, Norwood K, Assié A, et al. Acute high-fat diet impairs macrophage-supported intestinal damage resolution. JCI Insight. 2023; 8: e164489. https://doi.org/10.1172/jci.insight.164489

[37] Wu Y, Li J, Liu M, Gao R, Zhou H, Hu Q, et al. Extracellular Vesicles From LPS-Treated PDLSCs Induce NLRP3 Inflammasome Activation in Periodontitis. Oral Diseases. 2025; 31: 1277–1289. https://doi.org/10.1111/odi.15210

[38] Li Y, Chen H, Zhou S. Macrophages and Tissue Homeostasis: From Physiological Functions to Disease Onset. Frontiers in Bioscience (Landmark Edition). 2025; 30: 42706. https://doi.org/10.31083/FBL42706

[39] Xiao L, Qu M, Chen L, Xiang M, Long Q, Liu J, et al. TWEAK modulates the characteristics of periodontal ligament stem cells via the Fn14/NF-κB pathway. International Journal of Molecular Medicine. 2026; 57: 8. https://doi.org/10.3892/ijmm.2025.5679

[40] Liu X, Chen M, Luo J, Zhao H, Zhou X, Gu Q, et al. Immunopolarization-regulated 3D printed-electrospun fibrous scaffolds for bone regeneration. Biomaterials. 2021; 276: 121037. https://doi.org/10.1016/j.biomaterials.2021.121037

[41] Fan S, Tan Y, Yuan X, Liu C, Wu X, Dai T, et al. Regulation of the immune microenvironment by pioglitazone-loaded polylactic glycolic acid nanosphere composite scaffolds to promote vascularization and bone regeneration. Journal of Tissue Engineering. 2024; 15: 20417314241231452. https://doi.org/10.1177/20417314241231452

[42] Yang Y, Yao Z, Sun Y, Nie Y, Zhang Y, Li Z, et al. 3D-printed manganese dioxide incorporated scaffold promotes osteogenic-angiogenic coupling for refractory bone defect by remodeling osteo-regenerative microenvironment. Bioactive Materials. 2025; 44: 354–370. https://doi.org/10.1016/j.bioactmat.2024.10.019

[43] Cao G, Xu Q, Huang S, Dai D, Wang J, Li W, et al. B10 cells regulate macrophage polarization to alleviate inflammation and bone loss in periodontitis. Journal of Periodontology. 2025; 96: 355–368. https://doi.org/10.1002/JPER.24-0114

[44] Tang D, Xu Y, Huang Z, Xiao Z, Sun C, Li J, et al. Poly-l-lactic acid electrospun membrane with specific morphology promotes bone regeneration through macrophage reprogramming. Journal of Nanobiotechnology. 2026; 24: 197. https://doi.org/10.1186/s12951-026-04182-y

[45] Han X, Wang F, Ma Y, Lv X, Zhang K, Wang Y, et al. TPG-functionalized PLGA/PCL nanofiber membrane facilitates periodontal tissue regeneration by modulating macrophages polarization via suppressing PI3K/AKT and NF-κB signaling pathways. Materials Today. Bio. 2024; 26: 101036. https://doi.org/10.1016/j.mtbio.2024.101036

[46] Liao Z, Liang L, Fang H, Cui Y, Liang C, Huang G, et al. Exogenous M2 Macrophage-Loaded Scaffolds Promote Early Periodontal Regeneration by Improving Osteogenic Differentiation, Cell Homing, and Angiogenesis. Advanced Healthcare Materials. 2025; 14: e2501428. https://doi.org/10.1002/adhm.202501428

[47] Song W, Huang W, Du Z, Xiao C, Qu J, Xu W, et al. 4D-printed Fe3O4-PLLA scaffolds modulate osteoimmune microenvironment for oral bone repair. Materials Today. Bio. 2026; 36: 102691. https://doi.org/10.1016/j.mtbio.2025.102691

[48] Zhou H, Wu D, Cheng J, Liu Q, Wu X, Jiang B, et al. 3D-Printed Bone Scaffolds Promote Bone Regeneration Through a Multi-Stage Temporal Therapeutic Strategy. Biotechnology and Bioengineering. 2026; 123: 598–610. https://doi.org/10.1002/bit.70135

[49] Kang Y, Xu C, Meng L, Dong X, Qi M, Jiang D. Exosome-functionalized magnesium-organic framework-based scaffolds with osteogenic, angiogenic and anti-inflammatory properties for accelerated bone regeneration. Bioactive Materials. 2022; 18: 26–41. https://doi.org/10.1016/j.bioactmat.2022.02.012

[50] Zhou X, Qian Y, Chen L, Li T, Sun X, Ma X, et al. Flowerbed-Inspired Biomimetic Scaffold with Rapid Internal Tissue Infiltration and Vascularization Capacity for Bone Repair. ACS Nano. 2023; 17: 5140–5156. https://doi.org/10.1021/acsnano.3c00598

[51] Fan P, Liu Y, Qian X, Li J, Xu Y, Qiu X, et al. An intelligent nanoreservoir system promotes heart valve regeneration via ROS scavenging and immunomodulation. Bioactive Materials. 2026; 55: 205–223. https://doi.org/10.1016/j.bioactmat.2025.09.010

[52] Huang M, Zhang L, Cui J, Zhang M, Wang Z, Yu S, et al. 3D printing of GelMA/nanohydroxyapatite/melanin nanoparticles composite hydrogel scaffolds for bone regeneration through immunomodulation. International Journal of Biological Macromolecules. 2025; 306: 141453. https://doi.org/10.1016/j.ijbiomac.2025.141453

[53] Xie X, Zhang J, Shu J, Wu Z, Wang C, Gao Z, et al. Relieving oxidative stress microenvironment and promoting vascularized bone formation to treat femoral head necrosis using 3D-printed scaffold with ultralong-term multienzyme-like activity. Journal of Orthopaedic Translation. 2025; 53: 206–220. https://doi.org/10.1016/j.jot.2025.06.010

[54] Alarcón-Sánchez MA, Rodríguez-Montaño R, Mosaddad SA, Heboyan A. Levels of IL-1β, MMP-8, and MMP-9 in the Saliva of Subjects With Periodontitis: A Systematic Review and Meta-Analysis. Journal of Clinical Laboratory Analysis. 2025; 39: e70040. https://doi.org/10.1002/jcla.70040

[55] Wei S, Lin T, Sáenz-Ravello G, Gao H, Zhang Y, Tonetti MS, et al. Diagnostic accuracy of salivary active matrix metalloproteinase (aMMP)-8 point-of-care test for detecting periodontitis in adults: A systematic review and meta-analysis. Journal of Clinical Periodontology. 2024; 51: 1093–1108. https://doi.org/10.1111/jcpe.14000

[56] Moaven H, Giacaman A, Beltrán V, Sam YH, Betancur D, Mainas G, et al. Biomarker Expression of Peri-Implantitis Lesions before and after Treatment: A Systematic Review. International Journal of Environmental Research and Public Health. 2022; 19: 14085. https://doi.org/10.3390/ijerph192114085